Spin-orbit torque in chemically disordered and $L1_1$-ordered $Cu_{100-x}Pt_x$

Xinyu Shu,[1] Jing Zhou,[1] Jinyu Deng,[1] Weinan Lin,[1] Jihang Yu,[1] Liang Liu,[1] Chenghang Zhou,[1] Ping Yang,[1,2] and Jingsheng Chen[1,*]

[1]*Department of Materials Science and Engineering, National University of Singapore, Singapore 117576, Singapore*

[2]*Singapore Synchrotron Light Source (SSLS), National University of Singapore, 5 Research Link, Singapore 117603, Singapore*

(Received 22 May 2019; published 18 November 2019)

The binary alloys with heavy elements have been considered promising candidates for spin-orbit torque application due to the tunable spin Hall effect. In light of previous studies, the effect of crystalline structure on spin Hall effect in nonmagnetic alloys has not been thoroughly studied. Here, we present a systematic investigation of the spin-orbit torques in chemically disordered $Cu_{100-x}Pt_x$ and $L1_1$-$Cu_{50}Pt_{50}$ by the spin torque ferromagnetic resonance technique. The results indicate that both the atomic concentration and the degree of the chemical ordering substantially influence the spin-orbit torque efficiency of the CuPt alloys. In chemically disordered $Cu_{100-x}Pt_x$, the primary mechanism of spin Hall effect changes from extrinsic to intrinsic when the Pt concentration is increased to larger than 80%. In $L1_1$-$Cu_{50}Pt_{50}$ with weak chemical ordering, the side-jump and intrinsic mechanisms dominate, whereas the skew scattering mechanism dominates for strong chemical ordering. This work provides a perspective to control the spin-orbit torques in alloys.

DOI: 10.1103/PhysRevMaterials.3.114410

I. INTRODUCTION

The spin-orbit torque (SOT) has attracted increasing attention due to its potential application in energy-efficient devices [1]. The SOT comprises a dampinglike component, which can switch the magnetization of a ferromagnet [2–4], and a fieldlike component, which drives the magnetic precession [3,4]. In a ferromagnet/heavy metal (FM/HM) heterostructure, it is commonly believed that the SOT originates from the Rashba-Edelstein effect due to the inversion-symmetry breaking at the interface [5] and/or the spin Hall effect (SHE) arising from the strong spin-orbit coupling (SOC) in nonmagnetic HMs [2]. The Rashba-Edelstein effect at the interface between nonmagnetic HM and FM mainly exerts a fieldlike torque on magnetization to promote the precession [5,6]. In the scenario of the SOT from the SHE, spin current generated in the HM layer can be transferred to an adjacent FM layer and exerts a dampinglike torque on the magnetic moment to switch the magnetization of the FM [4]. This magnetization switching efficiency depends on the SOT efficiency (θ_{SH}), which incorporates the charge-to-spin conversion efficiency in the HM layer through the SHE and the spin transmission efficiency at the interface. Therefore, the investigation of large and tunable θ_{SH} is of critical importance for magnetization switching.

Extensive studies on the SHE in nonmagnetic HMs (such as Ta [3,7,8], Au [9,10], and Pt [11–13]) and alloys [1,14–17] have been carried out. The origin of the SHE has been attributed to three mechanisms: intrinsic, side jump, and skew scattering [2]. It is believed that the intrinsic SHE is proportional to Z^4, in which Z is atomic weight [2,9]. The extrinsic mechanism, including side jump and skew scattering, can be adjusted using crystalline defects [9,11,18] and impurities [1,14–17]. The introduction of defects and impurities would increase the probability of electron scattering inside the HM. As a result, the electrical resistivity (ρ_o) and thus θ_{SH} are enhanced according to their correlation $\theta_{SH} = \sigma_{SH}\rho_o$ (where σ_{SH} is the spin Hall conductivity) [2,7,9,14,18]. Based on this knowledge, researchers have succeeded in manipulating the θ_{SH} by changing the atomic composition in nonmagnetic alloys [1,14–17]. Given the strong correlation among the atomic composition, ρ_o and θ_{SH}, however, the understanding of the intrinsic and the extrinsic contributions to SHE in alloys is still vague.

Furthermore, ρ_o can be controlled by changing the degree of chemical ordering for single-crystalline alloys [19,20]. It is thus possible to modulate θ_{SH} by adjusting the degree of chemical ordering. To date, studies on the chemical-ordering-dependent SOT review that the magnetic structures of FMs [21,22] and antiferromagnets (AFMs) [23,24] can affect SOT generation. However, experimental evidence of chemical-ordering-dependent θ_{SH} in nonmagnetic alloys is still lacking.

In this work, θ_{SH} and ρ_o in the chemically disordered $Cu_{100-x}Pt_x$ and $L1_1$-$Cu_{50}Pt_{50}$ alloys are systematically studied. We used a spin torque ferromagnetic resonance (ST-FMR) technique to evaluate the θ_{SH} of $Cu_{100-x}Pt_x$ in $Cu_{100-x}Pt_x/Ni_{81}Fe_{19}$ [also known as Permalloy (Py)] bilayer. The results show that the θ_{SH} of CuPt alloys changes with ρ_o, which is influenced by both the atomic concentration and the degree of chemical ordering. Moreover, the mechanisms of SHE in $L1_1$-$Cu_{50}Pt_{50}$ and chemically disordered $Cu_{100-x}Pt_x$ are interpreted by analyzing the components of ρ_o using phenomenological models.

II. EXPERIMENTAL DETAILS

Three types of $Cu_{100-x}Pt_x$/Py bilayer samples were fabricated using DC magnetron sputtering, including chemically disordered polycrystalline $Cu_{100-x}Pt_x(11)$/Py(11), and

*Corresponding author: msecj@nus.edu.sg

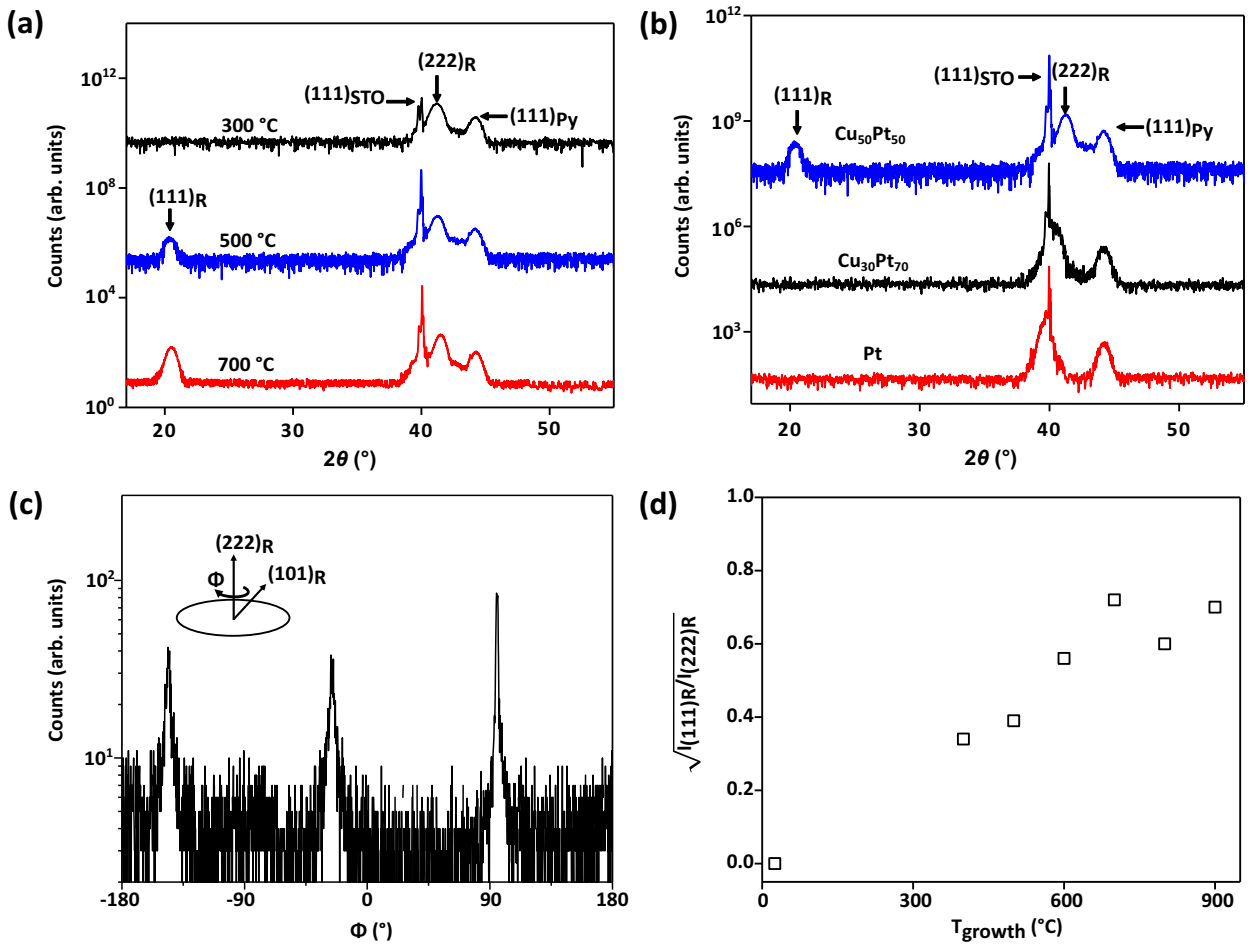

FIG. 1. (a) XRD θ-2θ results for $Cu_{50}Pt_{50}$/Py in which the $Cu_{50}Pt_{50}$ samples were prepared at 300 °C, 500 °C, and 700 °C. (b) XRD θ-2θ results for $Cu_{50}Pt_{50}$/Py, $Cu_{30}Pt_{70}$/Py, and Pt/Py in which the $Cu_{100-x}Pt_x$ layers were prepared at 500 °C. (c) The Φ-scan result of $L1_1$-$Cu_{50}Pt_{50}$ deposited at 500 °C. (d) The correlation between the square-rooted integrated intensity ratio of $I_{(111)R}$ over $I_{(222)R}$ and T_{grow}.

chemically disordered single-crystalline $Cu_{100-x}Pt_x$(11)/Py(11) and $L1_1$-$Cu_{50}Pt_{50}$(11)/Py(11). Numbers in the parentheses are the thicknesses in nanometers, which were measured by x-ray reflectometry. Polycrystalline $Cu_{100-x}Pt_x$ thin films were deposited on the thermally oxidized SiO_2 substrate at room temperature, while single-crystalline $Cu_{100-x}Pt_x$ films were epitaxially grown on $SrTiO_3$ (STO) (111) substrate at elevated temperatures. The Py layer was deposited at room temperature. All samples were protected by a 2-nm SiO_2 layer. The atomic composition of $Cu_{100-x}Pt_x$ was adjusted by changing the sputtering power and measured by energy-dispersive x-ray spectroscopy (EDS). The crystal structure of single-crystalline $Cu_{100-x}Pt_x$ was examined by x-ray diffraction (XRD). The devices for ST-FMR measurements were patterned by a combination of photolithography and ion-beam etching [25].

III. RESULTS AND DISCUSSION

Figure 1(a) shows the θ-2θ scans of $Cu_{50}Pt_{50}$(11)/Py(11) deposited on STO(111) substrates with $Cu_{50}Pt_{50}$ fabricated at different temperatures (T_{grow}). The peak at $2\theta = 20.31°$ corresponds to the (111) plane of the $L1_1$ superlattice in a rhombohedral structure denoted as $(111)_R$, while the peak at $2\theta = 41.17°$ corresponds to the first fundamental peak $(222)_R$. For $Cu_{50}Pt_{50}$ prepared at 500 °C and 700 °C, evident $(111)_R$ peaks can be observed. For $Cu_{50}Pt_{50}$ prepared at 300 °C, the $(111)_R$ peak disappears, which indicates the chemically disordered phase. There is no shift of $(222)_R$ peak position among those three $Cu_{50}Pt_{50}$ samples, which indicates the same atomic composition according to the Vegard's law. The peaks at $2\theta = 44.08°$ indicate the (111)-textured Py [26]. Figure 1(b) shows the θ-2θ scan of $Cu_{100-x}Pt_x$ deposited at 500 °C. The shift of the $(222)_R$ peak is attributed to composition changes. The (111) texture of Py is retained regardless of the Cu content. Figure 1(c) shows a typical Φ scan of $Cu_{100-x}Pt_x$ deposited at temperatures higher than 300 °C to confirm the epitaxial growth. A threefold symmetry consisting of $(101)_R$, $(011)_R$, and $(110)_R$ peaks around the $(222)_R$ peak is evident.

The long-range ordering parameter, which is defined as $S = \frac{r_A - c_A}{c_B}$ [19], quantifies the degree of chemical ordering of the $L1_1$-$Cu_{50}Pt_{50}$ films. Here, r_{Cu} stands for the fraction of Cu atoms on the correct atomic position to form the $L1_1$ structure, c_{Cu} and c_{Pt} are the atomic concentrations of Cu and Pt atoms. For the perfectly ordered $L1_1$ structure, $S = 1$, which means all the Cu and Pt atoms occupy their respective right position to form the $L1_1$ structure. In the case of perfectly

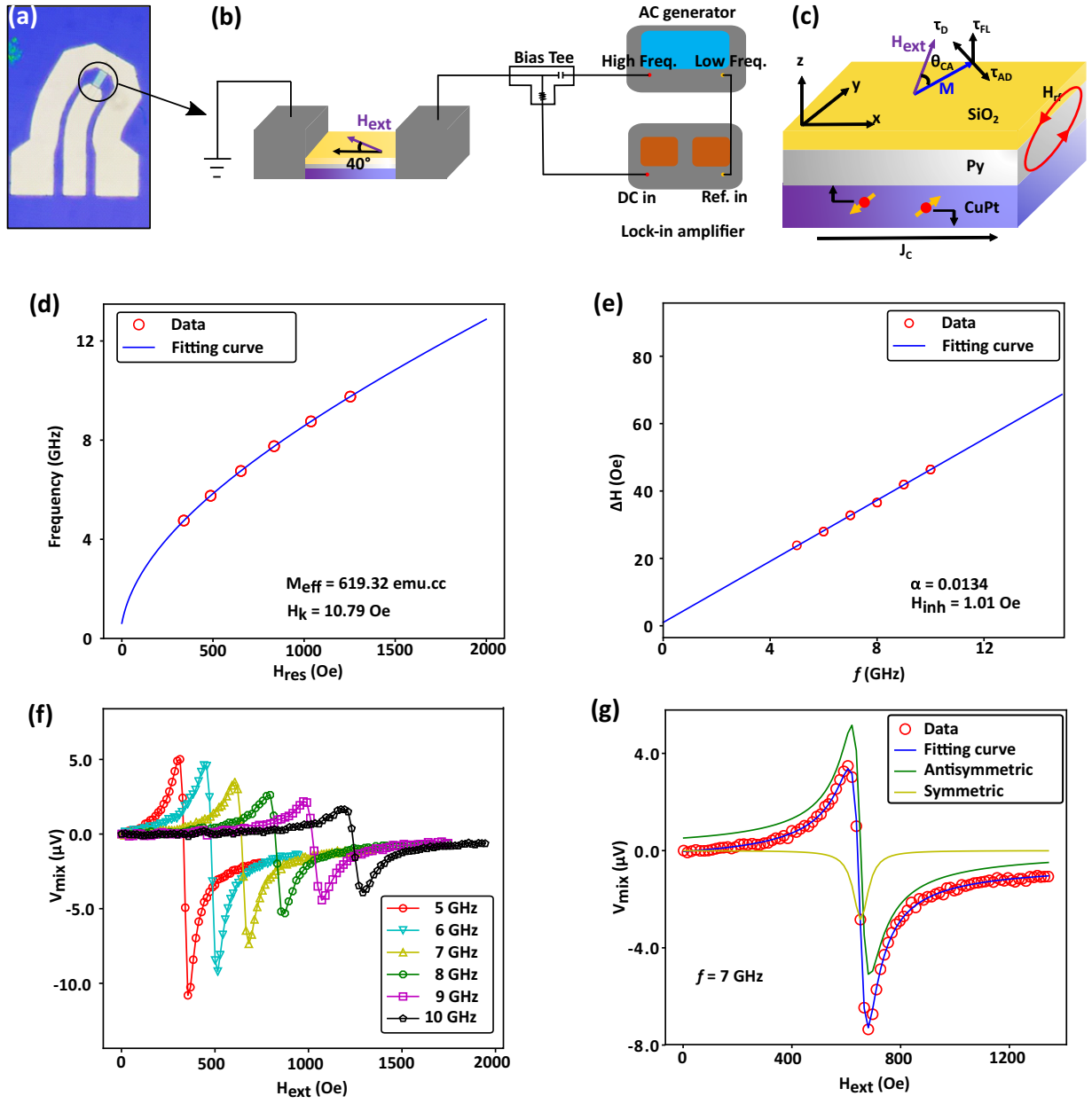

FIG. 2. (a)–(c) Illustrations for ST-FMR measurements. (d) Kittel fitting and (e) damping constant fitting of polycrystalline $Cu_{50}Pt_{50}(11)$/Py(11) for the ST-FMR measurements. (f) ST-FMR curves of polycrystalline $Cu_{50}Pt_{50}(11)$/Py(11) at different frequencies. (g) Decomposition of the ST-FMR curve which was measured at 7 GHz.

disordered CuPt, $S = 0$, where Cu and Pt atoms are completely random in the crystal lattice. Experimentally, S can be extracted from XRD θ-2θ curves as $S = C\sqrt{\frac{I_s}{I_o}}$, in which I_s is the integrated intensity of the first superlattice peak $[I_{(111)R}]$, and I_o is the integrated intensity of the first fundamental peak $[I_{(222)R}]$. C is a constant, including the Lorentz polarization factor and the structure factor [27]. The dependence of $\sqrt{\frac{I_s}{I_o}}$ on T_{grow} for $Cu_{50}Pt_{50}$ is summarized in Fig. 1(d). The ratio $\sqrt{\frac{I_s}{I_o}}$, which is linear with S, shows a monotonic increase when T_{grow} increases from 300 °C to 700 °C. Further increasing T_{grow} to 900 °C leads to a slight decrease of chemical ordering.

ST-FMR measurements were performed upon the polycrystalline $Cu_{100-x}Pt_x$ and $L1_1$-$Cu_{50}Pt_{50}$, both of which were patterned into microstrips [highlighted by a black circle in Fig. 2(a)] with dimensions of $30 \times 150\,\mu$m. The external magnetic field H_{ext} was applied at 40° with respect to the direction of microwave in the sample plane [as shown in Fig. 2(b)]. The magnetic precession in the FM layer arises from the combined effects of antidamping torque (τ_{AD}), damping torque (τ_D), and fieldlike torque (τ_{FL}) [see Fig. 2(c)]. For the bilayer heterostructure composed by nonmagnetic HM and FM, the traditional ST-FMR model attributes τ_{AD} to the SHE and τ_{FL} to the Oersted field [3]. The τ_{FL} from the Rashba-Edelstein effect is believed to be negligible [3,4]. The magnetic precession

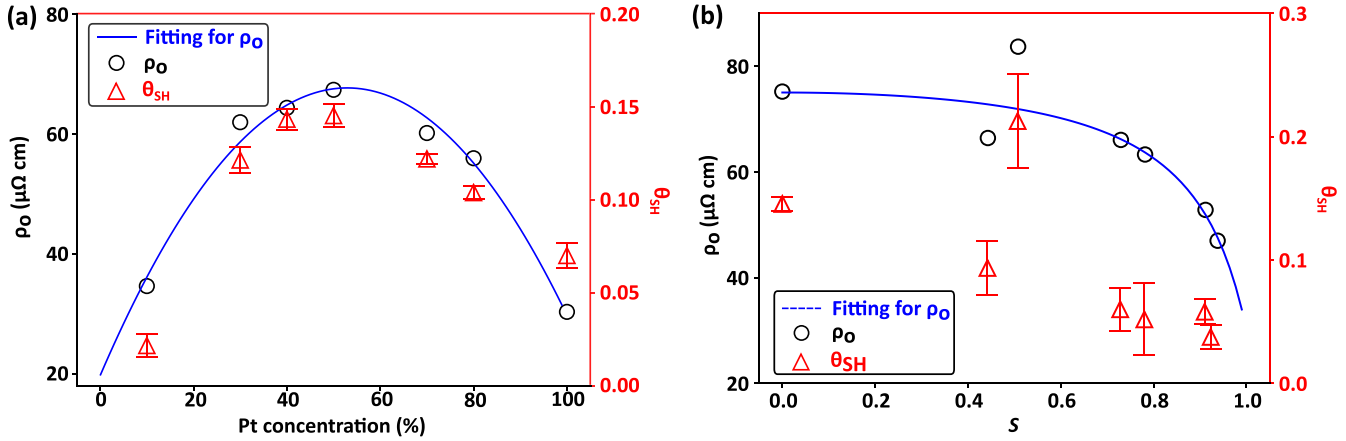

FIG. 3. (a) θ_{SH} and ρ_o in polycrystalline $Cu_{100-x}Pt_x(11)$/Py(11), and (b) θ_{SH} and ρ_o in $L1_1$-$Cu_{50}Pt_{50}(11)$/Py(11).

leads to alternating resistance due to the anisotropic magnetoresistance effect of the FM layer. A rectifying DC voltage $V_{\rm mix}$ can arise from mixing the alternating resistance and alternating current. $V_{\rm mix}$ can be decomposed into a symmetric component $Vs = \Delta H/[\Delta H^2 + (H_{\rm ext} - H_{\rm res})^2]$ (corresponding to τ_{AD}) and an antisymmetric component $V_A = \Delta H(H_{\rm ext} - H_{\rm res})/[\Delta H^2 + (H_{\rm ext}H_{\rm res})^2]$ (corresponding to τ_{FL}) [3,22], where $H_{\rm res}$ is the resonant field and ΔH is the half-width at half maximum of the ST-FMR curve. Finally, θ_{SH} is expressed as $\theta_{SH} = (V_S/V_A)(e\mu_o M_s t d/\hbar)[1 + (4\pi M_{\rm eff}/H_{\rm res})]^{1/2}$ [3,24], where M_s and $M_{\rm eff}$ are saturation and effective magnetization of the FM layer, respectively. $\hbar$ is the reduced Plank constant, and t and d are thicknesses of the FM and HM layers, respectively. It should be noted that the measured θ_{SH} corresponds to the lower boundary of the spin Hall angle due to the loss of spin current density at the interface during the spin transfer process.

We exemplify a full set of ST-FMR results of polycrystalline $Cu_{50}Pt_{50}(11)$/Py(11) in Figs. 2(d)–2(g). The resonant frequency f is fitted against $H_{\rm res}$ using the Kittel equation $f = (\gamma/2\pi)[(H_{\rm res} + H_k)(H_{\rm res} + H_k + 4\pi M_{\rm eff})]^{1/2}$, where γ is the gyromagnetic ratio and H_k is the in-plane effective anisotropic field [28]. In Fig. 2(d), $M_{\rm eff}$ and H_k are fitted as 619.32 emu.cc and 10.79 Oe, respectively. The damping constant α can be extracted through $\Delta H = \Delta H_{\rm inhom} + 2\pi\alpha f/\gamma$, where $\Delta H_{\rm inhom}$ is the inhomogeneous linewidth broadening [28], as shown in Fig. 2(e). Figure 2(f) presents $H_{\rm ext}$-$V_{\rm mix}$ curves obtained at different frequencies. A further decomposition of $V_{\rm mix}$ at $f = 7$ GHz is shown in Fig. 2(g). In this paper, the θ_{SH} for each sample is averaged at four different frequencies (6.5, 7, 7.5, and 8 GHz).

The effects of atomic concentration and chemical ordering on the θ_{SH} of CuPt are displayed in Fig. 3. Note that the θ_{SH} has been calibrated considering interfacial transparency (see details in the Supplemental Materials, Sec. I [29]). In order to understand the mechanisms of SHE, ρ_o of all the single-layer CuPt was measured by four-probe technique to study its correlation with θ_{SH} [7–13]. In Fig. 3(a), ρ_o of polycrystalline $Cu_{100-x}Pt_x$ can be well fitted against $c_{\rm Pt}$ using Nordheim's rule as expressed by Eq. (1) [14]. Figure 3(b) presents the dependence of ρ_o on the degrees of chemical ordering in $L1_1$-$Cu_{50}Pt_{50}$, which is fitted by Rossiter's model in Eq. (2) [19,20]:

$$\rho_o = Ac_{\rm Pt}c_{\rm Cu} + c_{\rm Pt}\rho_{\rm Pt} + c_{\rm Cu}\rho_{\rm Cu}, \tag{1}$$

$$\rho_o = \rho_{{\rm dis},r}\frac{1 - \left(C\sqrt{\frac{I_s}{I_o}}\right)^2}{1 - B\left(C\sqrt{\frac{I_s}{I_o}}\right)^2} + \rho_T. \tag{2}$$

In Eq. (1), A is the Nordheim coefficient, and $\rho_{\rm Cu}$ and $\rho_{\rm Pt}$ are the resistivity of Cu and Pt, respectively. The fitting results are $A = 171.01\,\mu\Omega\,$cm, $\rho_{\rm Pt} = 29.74\,\mu\Omega\,$cm, and $\rho_{\rm Cu} = 19.69\,\mu\Omega\,$cm. According to Nordheim's rule, the residual resistivity ρ_r is conveyed as $Ac_{\rm Pt}c_{\rm Cu}$ and the temperature-dependent ρ_T is described as $c_{\rm Pt}\rho_{\rm Pt} + c_{\rm Cu}\rho_{\rm Cu}$ [20]. In Eq. (2), C can be obtained by fitting in order to calculate S. The constant B, which is also fitted, depends on the relative position of the Fermi surface and the superlattice Brillouin-zone boundaries [19]. $\rho_{{\rm dis},r}$ is the residual resistivity of perfectly disordered $Cu_{50}Pt_{50}$ (i.e., $S = 0$), and the term $\rho_{{\rm dis},r}\frac{1-S^2}{1-BS^2}$ stands for the ρ_r of $Cu_{50}Pt_{50}$ with different degrees of chemical ordering. The measured ρ_o of $L1_1$-$Cu_{50}Pt_{50}$ with $S = 0.46$ deviates from the fitting, which can be attributed to the effect of short-range ordering [20]. From fitting, $\rho_{{\rm dis},r} = 44.93\,\mu\Omega\,$cm, $\rho_T = 30.08\,\mu\Omega\,$cm, $C = 1.3$, and $B = 0.78$.

Figure 3 exhibits an evident correlation between θ_{SH} and ρ_o in polycrystalline $Cu_{100-x}Pt_x$ and $L1_1$-$Cu_{50}Pt_{50}$, regardless of how ρ_o is modulated. In polycrystalline $Cu_{100-x}Pt_x$, both the θ_{SH} and ρ_o present a parabolic trend with the maxima at $c_{\rm Pt} = 50\%$, where $\theta_{SH} = 0.1452$ and $\rho_o = 67.3\,\mu\Omega\,$cm. On the other hand, the $L1_1$-$Cu_{50}Pt_{50}$ displays negative dependence of θ_{SH} on S. Unlike the cases in FM [21] and AFM materials [24], where dramatic changes in θ_{SH} are observed with simultaneous changes in crystal and magnetic structures, θ_{SH} of $L1_1$-$Cu_{50}Pt_{50}$ can be modified by tuning the crystal structure alone, as represented by the differed degree of chemical ordering.

In light of the single-element HMs, the correlation between θ_{SH} and ρ_o can be explained by the intrinsic and extrinsic contributions to spin Hall resistivity ρ_{SH} [7–9,18]. However, the correlation between θ_{SH} and ρ_o in nonmagnetic binary

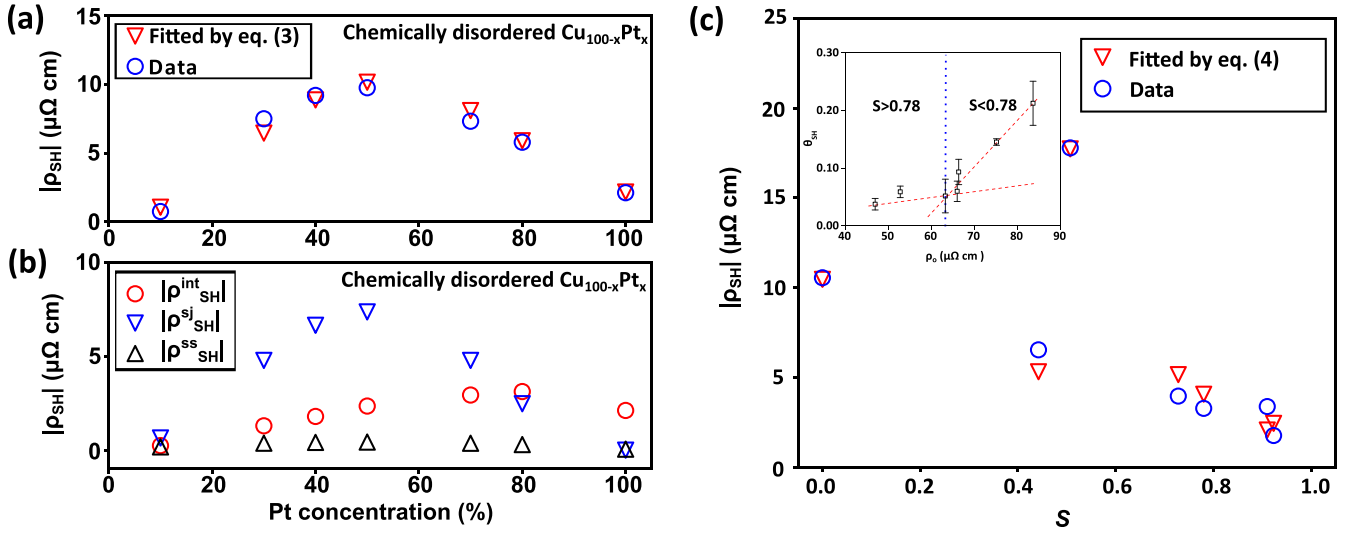

FIG. 4. (a) Correlation between ρ_{SH} and c_{Pt} in polycrystalline $Cu_{100-x}Pt_x$ and fitting results by applying Eq. (3). (b) Calculated intrinsic and extrinsic spin Hall resistivity including the side-jump and skew scattering contributions. (c) Correlation between ρ_{SH} and S in $L1_1$-$Cu_{50}Pt_{50}$ and fitting results by applying Eq. (4). The inset in (c) shows the change of θ_{SH} with ρ_o. Two dependences of θ_{SH} on ρ_o are visually guided by the red dashed lines. A blue dotted line marks the crossover of these two dependences, which corresponds to $S = 0.78$.

alloys is more complicated due to the effects of the atomic concentration and the chemical ordering. Here we develop two models to understand the correlations between ρ_o and θ_{SH} in polycrystalline $Cu_{100-x}Pt_x$ and $L1_1$-$Cu_{50}Pt_{50}$, respectively:

$$-\rho_{SH} = \left(\theta^{\rm int}_{SH,Cu} c{\rm Cu} + \theta^{\rm int}_{SH,Pt} c{\rm Pt}\right)\rho_o + \sigma^{sj}_{SH}\,(c{\rm Pt})\,\rho_r^2 + \theta^{ss,T}_{SH}\rho_T + \theta^{ss,{\rm imp}}_{SH}\rho_r, \quad (3)$$

$$-\rho_{SH} = \sigma^{\rm int}_{SH}(S)\,(\rho_r+\rho_T)^2 + \sigma^{sj}_{SH}(S)\,\rho_r^2 + \theta^{ss,T}_{SH}\rho_T + \theta^{ss,{\rm imp}}_{SH}\rho_r. \quad (4)$$

Equation (3) describes ρ_{SH} of polycrystalline $Cu_{100-x}Pt_x$. Here, the $\theta^{\rm int}_{SH,Cu} = 0$ and $\theta^{\rm int}_{SH,Pt} = 0.07$ are the intrinsic SOT efficiencies of Cu and Pt, respectively. $\sigma^{sj}_{SH}\,(c_{Pt})$ stands for the concentration-dependent side-jump spin Hall conductivity. $\theta^{ss,{\rm imp}}_{SH}$ and $\theta^{ss,T}_{SH}$ are impurity-dependent and temperature-dependent components of skew scattering-induced SOT efficiency, respectively [30]. The detailed construction of Eq. (3) is discussed in the Supplemental Material, Sec. II. Equation (4) depicts ρ_{SH} of $L1_1$-$Cu_{50}Pt_{50}$. In the $L1_1$-$Cu_{50}Pt_{50}$, the degree of chemical ordering is deemed to strongly affect the electronic band structure [31,32]. Therefore, $\sigma^{\rm int}_{SH}(S)$ and $\sigma^{sj}_{SH}(S)$ stand for the S-dependent intrinsic and side-jump σ^{sj}_{SH}, respectively.

The effects of atomic concentration and chemical ordering on the ρ_{SH} of CuPt are well fitted by Eqs. (3) and (4), as shown in Fig. 4. Figure 4(a) presents both the fitting results and data of polycrystalline $Cu_{100-x}Pt_x$. The side-jump spin Hall conductivity $\sigma^{sj}_{SH}(c_{Pt})$ is approximated as $(ac_{Pt} + b)$ [33]. The fitted parameters from Eq. (3) are $\theta^{ss,T}_{SH} = 0.0016$, $\theta^{ss,{\rm imp}}_{SH} = 0.01$, $a = 4.73 \times 10^{-5}\,\mu\Omega\,{\rm cm}$, and $b = 0.002\,\mu\Omega\,{\rm cm}$ for the polycrystalline $Cu_{100-x}Pt_x$. The contributions from different mechanisms are plotted in Fig. 4(b), where $|\rho^{\rm int}_{SH}| = (\theta^{\rm int}_{SH,Cu} c{\rm Cu} + \theta^{\rm int}_{SH,Pt} c_{Pt})\rho_o$, $|\rho^{SJ}_{SH}| = \sigma^{sj}_{SH}\,(c_{Pt})\,\rho_r^2$, and $|\rho^{SS}_{SH}| = \theta^{ss,T}_{SH}\rho_T + \theta^{ss,{\rm imp}}_{SH}\rho_r$, corresponding to intrinsic, side jump, and skew scattering ρ_{SH}, respectively. When $c_{Pt} < 80\%$, the side-jump contribution dominates the ρ_{SH}. When $c_{Pt} > 80\%$, the intrinsic contribution overwhelms the extrinsic contribution. The maximum of ρ_{SH} in Fig. 4(a), as well as the maximum of θ_{SH} in Fig. 3(a), can be attributed to the dominant role of the side-jump mechanism, which is also maximum at $c_{Pt} = 50\%$ in Fig. 4(b).

Figure 4(c) shows the data of $L1_1$-$Cu_{50}Pt_{50}$ and its fit through Eq. (4), where we approximately take $\sigma^{\rm int}_{SH}(S)$ and $\sigma^{sj}_{SH}(S)$ as two constants. The well-fitted results verify the validity of Eq. (4). In light of the $\sigma^{sj}_{SH}(S)\,\rho_r^2$ in Eq. (4), the negative dependence of θ_{SH} on S in Fig. 3(b) can be attributed to the decrease of the side-jump contribution in $L1_1$-$Cu_{50}Pt_{50}$ with increasing S. In a perfectly ordered $L1_1$-$Cu_{50}Pt_{50}$, the crystalline structure acts as a translationally invariant configuration in which the electron scattering at impurities, as well as ρ_r, is negligible [19,20]. Therefore, it is expected that the ρ_r, as well as the side-jump contribution, reduces with increasing S in $L1_1$-$Cu_{50}Pt_{50}$. Additionally, when $S \geqslant 0.78$, the decrease of ρ_o is much faster than the reduction in θ_{SH}, where θ_{SH} is almost independent of ρ_o, as shown in the inset in Fig. 4(c). This implies that there is a threshold value of S at around 0.78 above which the dominant spin Hall mechanism changes from side jump and intrinsic to skew scattering in $L1_1$-$Cu_{50}Pt_{50}$.

IV. CONCLUSION

In summary, the SOTs of chemically disordered polycrystalline $Cu_{100-x}Pt_x$ and $L1_1$-$Cu_{50}Pt_{50}$ were investigated systematically in this work. We demonstrate that both the atomic composition and the chemical order can strongly influence the θ_{SH} in CuPt alloy. In chemically disordered $Cu_{100-x}Pt_x$, the primary spin Hall mechanism changes from a side-jump to intrinsic mechanism when c_{Pt} increases to larger than 80%. The dominance of the side-jump mechanism accounts for

the maximum of θ_{SH} and ρ_{SH} at Pt concentration of 50%. In $L1_1$-$Cu_{50}Pt_{50}$, there appears to be a threshold value of S at around 0.78, which corresponds to the transition of the dominant mechanism of the SHE, from side jump and intrinsic to skew scattering.

Note added. We noticed that the dependence of θ_{SH} on the Pt concentration in our work is different from the results in a previous paper [14] in which the θ_{SH} saturates at certain Pt concentrations. Such a difference may arise from different considerations of the interfacial transparency. As addressed in the Supplemental Material, Sec. I [29], the dependence of θ_{SH} on Pt concentration may be significantly influenced by the interfacial transparency, which is neglected in Ref. [14]. Furthermore, the elemental segregation of Pt as mentioned in Ref. [14] can also lead to a different θ_{SH} from that of the homogeneous solid solution. The preferential distribution of Pt can lead to the drop of resistivity and thereby a decrease of θ_{SH}. These two factors can possibly result in the different dependences of θ_{SH} on Pt concentration.

ACKNOWLEDGMENTS

We gratefully acknowledge support from the Singapore National Research Foundation under CRP Award No. NRF-CRP10-2012-02, and the Singapore Ministry of Education MOE2018-T2-2-043, AMEIRG18-0022, A*STAR IAF-ICP 11801E0036, and MOE Tier 1- FY2018–P23. We thank the Singapore Synchrotron Light Source (SSLS) for providing the necessary facility. P.Y. was supported by the SSLS via NUS Core Support C-380-003-003-001.

X.S. constructed the main part of this project and operated most of the experiments. J.C. supervised the experiment and manuscript. J.Z. built up the ST-FMR measurement platform and helped analyze the ST-FMR results. J.D. helped analyze the XRD results. W.L. and L.L. helped to revise the manuscript. J.Y. and C.Z. helped fabricate devices. P.Y. helped to measure the x-ray reflection and Φ scan. All authors contributed to the discussion and final version of the manuscript.

The authors declare no competing interests.

[1] L. K. Zou, S. H. Wang, Y. Zhang, J. R. Sun, J. W. Cai, and S. S. Kang, Large extrinsic spin Hall effect in Au-Cu alloys by extensive atomic disorder scattering, Phys. Rev. B **93**, 014422 (2016).

[2] J. Sinova, S. O. Valenzuela, J. Wunderlich, C. H. Back, and T. Jungwirth, Spin Hall effects, Rev. Mod. Phys. **87**, 1213 (2015).

[3] L. Liu, T. Moriyama, D. C. Ralph, and R. A. Buhrman, Spin-Torque Ferromagnetic Resonance Induced by the Spin Hall Effect, Phys. Rev. Lett. **106**, 036601 (2011).

[4] L. Liu, O. J. Lee, T. J. Gudmundsen, D. C. Ralph, and R. A. Buhrman, Current-Induced Switching of Perpendicularly Magnetized Magnetic Layers Using Spin Torque from the spin Hall effect, Phys. Rev. Lett. **109**, 096602 (2012).

[5] A. Manchon and S. Zhang, Theory of nonequilibrium intrinsic spin torque in a single nanomagnet, Phys. Rev. B **78**, 212405 (2008).

[6] I. M. Miron, K. Garello, G. Gaudin, P. J. Zermatten, M. V. Costache, S. Auffret, S. Bandiera, B. Rodmacq, A. Schuhl, and P. Gambardella, Perpendicular switching of a single ferromagnetic layer induced by in-plane current injection, Nature (London) **476**, 189 (2011).

[7] E. Sagasta, Y. Omori, S. Vélez, R. Llopis, C. Tollan, A. Chuvilin, L. E. Hueso, M. Gradhand, Y. Otani, and F. Casanova, Unveiling the mechanisms of the spin Hall effect in Ta, Phys. Rev. B **98**, 060410 (2018).

[8] A. Kumar, R. Bansal, S. Chaudhary, and P. K. Muduli, Large spin current generation by the spin Hall effect in mixed crystalline phase Ta thin films, Phys. Rev. B **98**, 104403 (2018).

[9] M. Isasa, E. Villamor, L. E. Hueso, M. Gradhand, and F. Casanova, Temperature dependence of spin diffusion length and spin Hall angle in Au and Pt, Phys. Rev. B **91**, 024402 (2015).

[10] M. Obstbaum, M. Härtinger, H. G. Bauer, T. Meier, F. Swientek, C. H. Back, and G. Woltersdorf, Inverse spin Hall effect in $Ni_{81}Fe_{19}$/normal-metal bilayers, Phys. Rev. B **89**, 060407 (2014).

[11] Y. Wang, P. Deorani, X. Qiu, J. H. Kwon, and H. Yang, Determination of intrinsic spin Hall angle in Pt, Appl. Phys. Lett. **105**, 152412 (2014).

[12] W. Zhang, W. Han, X. Jiang, S. H. Yang, and S. S. P Parkin, Role of transparency of platinum–ferromagnet interfaces in determining the intrinsic magnitude of the spin Hall effect, Nat. Phys. **11**, 496 (2015).

[13] C. F. Pai, Y Ou, L. H. Vilela-Leão, D. C. Ralph, and R. A. Buhrman, Dependence of the efficiency of spin Hall torque on the transparency of Pt/ferromagnetic layer interfaces, Phys. Rev. B **92**, 064426 (2015).

[14] R. Ramaswamy, Y. Wang, M. Elyasi, M. Motapothula, T. Venkatesan, X. Qiu, and H. Yang, Extrinsic Spin Hall Effect in $Cu_{1-x}Pt_x$, Phys. Rev. Appl. **8**, 024034 (2017).

[15] T. Y. Chen, C. T. Wu, H. Y. Yen, and C. F. Pai, Tunable spin-orbit torque in Cu-Ta binary alloy heterostructures, Phys. Rev. B **96**, 104434 (2017).

[16] D. Qu, S. Y. Huang, G. Y. Guo, and C. L. Chien, Inverse spin Hall effect in Au_xTa_{1-x} alloy films, Phys. Rev. B **97**, 024402 (2018).

[17] K. Fritz, S. Wimmer, H. Ebert, and M. Meinert, Large spin Hall effect in an amorphous binary alloy, Phys. Rev. B **98**, 094433 (2018).

[18] Y. Tian, L. Ye, and X. Jin, Proper Scaling of the Anomalous Hall Effect, Phys. Rev. Lett. **103**, 087206 (2009).

[19] H. Lang, T. Mohri, and W. Pfeiler, L11 Long-range order in CuPt: A comparison between x-ray and residual resistivity measurements, Intermetallics **7**, 1373 (1999).

[20] J. Banhart and G. Czycholl, Electrical conductivity of long-range–ordered alloys, Europhys. Lett. **58**, 264 (2002).

[21] Y. Ou, D. C. Ralph, and R. A. Buhrman, Strong Enhancement of the Spin Hall Effect by Spin Fluctuations Near the Curie Point of Fe_xPt_{1-x} Alloys, Phys. Rev. Lett. **120**, 097203 (2018).

[22] C. S. Kim, J. J. Sapan, S. Moyerman, K. Lee, E. E. Fullerton, and M. H. Kryder, Thickness and temperature effects on magnetic properties and roughness of L10-ordered FePt films, IEEE Trans. Magn. **46**, 2282 (2010).

[23] V. Tshitoyan, C. Ciccarelli, A. P. Mihai, M. Ali, A. C. Irvine, T. A. Moore, T. Jungwirth, and A. J. Ferguson, Electrical manipulation of ferromagnetic NiFe by antiferromagnetic IrMn, Phys. Rev. B **92**, 214406 (2015).

[24] J. Zhou, X. Wang, Y. Liu, J. Yu, H. Fu, L. Liu, S. Chen, J. Deng, W. Lin, X. Shu, H. Y. Yoong, T. Hong, M. Matsuda, P. Yang, S. Adams, B. Yan, X. Han, and J. S. Chen, Large spin-orbit torque efficiency enhanced by magnetic structure of collinear antiferromagnet IrMn, Sci. Adv. **5**, eaau6696 (2019).

[25] D. MacNeill, G. M. Stiehl, M. H. D. Guimaraes, R. A. Buhrman, J. Park, and D. C. Ralph, Control of spin-orbit torques through crystal symmetry in WTe_2/ferromagnet bilayers, Nat. Phys. **13**, 300 (2017).

[26] J. Fassbender, J. von Borany, A. Mücklich, K. Potzger, W. Möller, J. McCord, L. Schultz, and R. Mattheis, Structural and magnetic modifications of Cr-implanted Permalloy, Phys. Rev. B **73**, 184410 (2006).

[27] J. Deng, H. Li, K. Dong, R. W. Li, Y. Peng, G. Ju, J. Hu, G. M. Chow, and J. S. Chen, Lattice-Mismatch-Induced Oscillatory Feature Size and Its Impact on the Physical Limitation of Grain Size, Phys. Rev. Appl. **9**, 034023 (2018).

[28] J. Zhou, S. Chen, W. Lin, Q. Qin, L. Liu, S. He, and J. S. Chen, Effects of field annealing on Gilbert damping of polycrystalline CoFe thin films, J. Magn. Magn. Mater. **441**, 264 (2017).

[29] See Supplemental Material at http://link.aps.org/supplemental/10.1103/PhysRevMaterials.3.114410 for the consideration of interfacial transparency and detailed constructions of the empirical model.

[30] G. V. Karnad, C. Gorini, K. Lee, T. Schulz, R. Lo Conte, A. W. J. Wells, D. S. Han, K. Shahbazi, J. S. Kim, T. A. Moore, H. J. M. Swagten, U. Eckern, R. Raimondi, and M. Kläui, Evidence for phonon skew scattering in the spin Hall effect of platinum, Phys. Rev. B **97**, 100405 (2018).

[31] L. J. Zhu, D. Pan, and J. H. Zhao, Anomalous Hall effect in epitaxial $L1_0$-$Mn_{1.5}Ga$ films with variable chemical ordering, Phys. Rev. B **89**, 220406 (2014).

[32] A. F. Wright, K. Leung, and M. V. Schilfgaarde, Effects of biaxial strain and chemical ordering on the band gap of InGaN, Appl. Phys. Lett. **78**, 189 (2001).

[33] P. He, L. Ma, Z. Shi, G. Y. Guo, J. G. Zheng, Y. Xin, and S. M. Zhou, Chemical Composition Tuning of the Anomalous Hall Effect in Isoelectronic $L1_0$ $FePd_{1-x}Pt_x$ Alloy Films, Phys. Rev. Lett. **109**, 066402 (2012).